Astronomy & Astrophysics manuscript no. Marulli
March 12, 2013

© ESO 2013

arXiv:1303.2633v1 [astro-ph.CO] 11 Mar 2013

The VIMOS Public Extragalactic Redshift Survey (VIPERS) ⋆

Luminosity and stellar mass dependence of galaxy clustering at $0.5 < z < 1.1$

F. Marulli[1,2,3], M. Bolzonella[2], E. Branchini[4,5,6], I. Davidzon[1,2], S. de la Torre[7], B. R. Granett[8], L. Guzzo[8,9], A. Iovino[8], L. Moscardini[1,2,3], A. Pollo[10,11], U. Abbas[12], C. Adami[13], S. Arnouts[13,14], J. Bel[15], D. Bottini[16], A. Cappi[2,17], J. Coupon[18], O. Cucciati[2], G. De Lucia[19], A. Fritz[16], P. Franzetti[16], M. Fumana[16], B. Garilli[13,16], O. Ilbert[13], J. Krywult[20], V. Le Brun[13], O. Le Fèvre[13], D. Maccagni[16], K. Małek[21], H. J. McCracken[22], L. Paioro[16], M. Polletta[16], H. Schlagenhaufer[23,24], M. Scodeggio[16], L. A. M. Tasca[13], R. Tojeiro[25], D. Vergani[26], A. Zanichelli[27], A. Burden[25], C. Di Porto[2], A. Marchetti[8,28], C. Marinoni[15], Y. Mellier[22], R. C. Nichol[25], J. A. Peacock[7], W. J. Percival[25], S. Phleps[24], M. Wolk[22], and G. Zamorani[2]

(Affiliations can be found after the references)

Received –; accepted –

ABSTRACT

Aims. We investigate the dependence of galaxy clustering on luminosity and stellar mass, in the redshift range $0.5 < z < 1.1$, using the first ~ 55000 redshifts from the VIMOS Public Extragalactic Redshift Survey (VIPERS).

Methods. To characterize the spatial properties of the VIPERS galaxies, we measure the redshift-space two-point correlation functions (2PCF), $\xi(s)$ and $\xi(r_p, \pi)$, and the projected correlation function, $w_p(r_p)$, in samples covering different ranges of B-band absolute magnitudes and stellar masses. We consider both threshold and binned galaxy samples, with median B-band absolute magnitudes $-21.6 \lesssim M_B - 5\log(h) \lesssim -19.5$ and median stellar masses $9.8 \lesssim \log(M_\star[h^{-2}\, M_\odot]) \lesssim 10.7$. We assess the real-space clustering in the data from the projected correlation function, that we model as a power-law in the range $0.2 < r_p[h^{-1}\,\mathrm{Mpc}\,] < 20$. Finally, we estimate the galaxy bias as a function of luminosity, stellar mass and redshift, assuming a flat Λ cold dark matter model to derive the dark matter 2PCF.

Results. We provide the best-fit parameters of the power-law model assumed for the real-space 2PCF – the correlation length, r_0, and the slope, γ – as well as the linear bias parameter, as a function of the B-band absolute magnitude, stellar mass and redshift. We find a clear luminosity and stellar mass dependence of the galaxy clustering at all redshifts, with more luminous and massive galaxies showing a higher clustering amplitude, in agreement with previous studies. Our analysis provides new constraints on galaxy formation models that now have to match the observed redshift evolution of the clustering of VIPERS galaxies in a broad range of luminosity and stellar masses, between $z = 0.5$ and $z = 1.1$.

Key words. Cosmology: observations – Cosmology: large-scale structure of Universe – Surveys – Galaxies: evolution

1. Introduction

The Large Scale Structure (LSS) of the Universe contains fundamental information to investigate the nature of the dark matter (DM) and the origin of the accelerated expansion of the Universe. However, since the LSS is traced by galaxies, the relevant information can only be extracted after specifying the mapping between galaxies and DM. The way galaxies trace the underlying density field, i.e. their biasing, can be understood through the mean occupation of galaxies in DM haloes, under the assumption that all DM mass in the Universe is in the form of haloes.

Indeed, it has been observationally established in the local Universe that the spatial distribution of galaxies significantly depends on their luminosity, stellar mass, colour, morphological and spectral types, and on the environment (see e.g. Davis & Geller 1976; Giovanelli et al. 1986; Davis et al. 1988; Hamilton 1988; Einasto 1991; Maurogordato & Lachieze-Rey 1991; Loveday et al. 1995; Benoist et al. 1996; Guzzo et al. 1997, 2000; Willmer et al. 1998; Brown et al. 2000, 2003; Norberg et al. 2001, 2002; Zehavi et al. 2002, 2005; Madgwick et al. 2003; Abbas & Sheth 2006; Zehavi et al. 2011; Budavári et al. 2003; Li et al. 2006; Swanson et al. 2008; Loh et al. 2010; Ross et al. 2011; Guo et al. 2012; Christodoulou et al. 2012). The general trend is that luminous and massive galaxies with bulge-dominated morphologies and red colours cluster more strongly than faint, less massive, blue, spiral galaxies, an effect that becomes particularly evident above the characteristic luminosity, $L^\star$, and stellar mass, $M^\star$, of the Schechter function. This is expected in the standard cosmological scenario of hierarchical growth of cosmic structures, where bright galaxies are hosted by massive,

---

Send offprint requests to: F.Marulli
e-mail: `federico.marulli3@unibo.it`

⋆ Based on observations collected at the European Southern Observatory, Paranal, Chile under programs 182.A-0886 (LP) at the Very Large Telescope, and also based on observations obtained with MegaPrime/MegaCam, a joint project of CFHT and CEA/DAPNIA, at the Canada-France-Hawaii Telescope (CFHT), which is operated by the National Research Council (NRC) of Canada, the Institut National des Science de l'Univers of the Centre National de la Recherche Scientifique (CNRS) of France, and the University of Hawaii. This work is based in part on data products produced at TERAPIX and the Canadian Astronomy Data Centre as part of the Canada-France-Hawaii Telescope Legacy Survey, a collaborative project of NRC and CNRS. The VIPERS web site is http://vipers.inaf.it/.

rare and highly clustered DM haloes (White et al. 1987; Kaiser 1987).

Observations up to intermediate redshifts, $z \sim 1$, i.e. halfway through the cosmic time from the microwave background to the present, show clustering trends similar to those observed in the local Universe, with the more luminous and massive galaxies being more clustered than the faint, less massive ones (see e.g. Coil et al. 2006, 2008; McCracken et al. 2008; Meneux et al. 2006, 2008, 2009; Pollo et al. 2006; Abbas et al. 2010; Mostek et al. 2012). At higher redshifts, $z > 1$, observational constraints are generally weaker, suffering from a combination of many types of selection biases, but the measurements still show a luminosity and stellar mass segregation in galaxy clustering (see e.g. Daddi et al. 2003; Adelberger et al. 2005; Ouchi et al. 2005; Lee et al. 2006, 2009; Hildebrandt et al. 2009; Wake et al. 2011; Lin et al. 2012), with strong evidence for a steepening of the correlation function at $r \lesssim 1h^{-1}$ Mpc with increasing luminosity.

It is possible to derive cosmological constraints from the spatial properties of galaxies using methods that do not explicitly depend on galaxy bias, e.g. by exploiting baryonic acoustic oscillations (see e.g. Eisenstein et al. 2005; Cole et al. 2005; Percival et al. 2007, 2010) or geometric clustering distortions (see e.g. Alcock & Paczynski 1979; Simpson & Peacock 2010; Marulli et al. 2012), or by combining the one- and two-point moments of the smoothed galaxy density distribution (Bel et al. 2013). However, to extract the full information encoded in the shape of the galaxy power spectrum and in its redshift-space distortions, the galaxy bias must be accounted for to some extent. Since the connection between baryons and DM can be significantly affected by non-linear phenomena, such as mergers, dynamical friction, cooling, feedback, etc., semi-analytic models or full hydrodynamic simulations provide useful tools to properly investigate how galaxies trace the DM distribution. Once a mathematical description of the galaxy bias has been obtained, cosmological constraints can be derived by marginalising over the uncertain parameters describing the bias. Alternatively, observational measurements of the galaxy bias, derived in a given cosmological framework, can be used to constrain the parameters of galaxy formation models.

In this paper, we focus on the dependence of galaxy clustering on luminosity and stellar mass, providing new observational constraints at redshift $0.5 < z < 1.1$, from the first data release of the ongoing VIMOS Public Extragalactic Redshift Survey (VIPERS, Guzzo et al. 2013). The comparison between VIPERS clustering measurements with similar ones at lower and higher redshifts can constrain the cosmic evolution of the relationship between DM and galaxy properties, and therefore between gravity and cosmology on one side and processes associated with baryonic physics on the other side. The large number of objects with accurate spectroscopic redshifts and the large volume covered by the VIPERS survey give us the opportunity to measure the clustering of galaxies over a wide range of luminosities and stellar masses, up to the cosmic epoch when the Universe was still decelerating. In particular, we provide constraints on the projected correlation function, that we model as a single power-law. This represents a reasonable, though not optimal, approximation at $r_p \lesssim 20h^{-1}$ Mpc, where r_p is the direction perpendicular to the line-of-sight, and facilitates the comparison with previous studies. A more detailed interpretation of these data using Halo Occupation Distribution (HOD) modelling is deferred to a future work (see also de la Torre et al. 2013).

The plan of this paper is as follows. In Section 2 we give a general overview of the VIPERS data, describing in detail the luminosity and stellar mass selections adopted in this work. We investigate the spatial distribution of VIPERS galaxies measuring the two-point correlation function (2PCF) in approximately volume-limited samples of different B-band absolute magnitude and stellar mass. The methodology of this analysis is described in Section 3, where we also explain how we account for the incompleteness affecting our VIPERS sample. More technical details about the method used to correct for the proximity effect and stellar mass incompleteness are provided in Appendix A. The results of our analysis are presented in Section 4. Finally, in Section 5 we summarize the main results of this analysis.

Throughout this paper, we assume a flat Λ cold dark matter (CDM) background cosmology, with mass density parameter $\Omega_M = 0.25$, both to convert the measured redshifts into comoving distances and to estimate the DM correlation used to assess the galaxy bias. Changing the value of Ω_M in a reasonable range, given the current cosmological constraints, would introduce only small effects on our clustering measurements within their observational uncertainties (see e.g. Marulli et al. 2012). Galaxy magnitudes are quoted in the AB system. The dependence of observed quantities on the Hubble parameter is indicated as a function of $h \equiv H_0/100\,\mathrm{km\,s^{-1}Mpc^{-1}}$.

2. The data

2.1. The VIPERS survey

We investigate the luminosity and stellar mass dependence of galaxy clustering using the VIPERS Public Data Release 1 (PDR-1), that will be made publicly available in the fall of 2013. VIPERS is an ongoing Large Programme aimed at measuring redshifts for $\sim 10^5$ galaxies at $0.5 < z \lesssim 1.2$. One of the main goals of this survey is to characterize the galaxy spatial properties and growth rate of the LSS, measuring galaxy clustering and redshift-space distortions at an epoch when the Universe was about half its current age. Indeed, according to the standard ΛCDM scenario, the redshift range that VIPERS probes is previous to the dark energy (DE) dominated era, crossing the cosmic epoch when the Universe started accelerating (see the bottom labels in Fig. 1).

The galaxy target sample is selected from the Canada-France-Hawaii Telescope Legacy Survey Wide (CFHTLS-Wide) optical photometric catalogues (Mellier et al. 2008). VIPERS covers ~ 24 deg^2 on the sky, divided over two areas within the W1 and W4 CFHTLS fields. Galaxies are selected down to a flux limit of $i_{AB} < 22.5$, and a robust *gri* colour pre-selection is applied to effectively remove objects at $z < 0.5$. Coupled with an aggressive observing strategy (Scodeggio et al. 2009), this allows us to double the galaxy sampling rate in the redshift range of interest ($\sim 40\%$), with respect to a pure magnitude-limited sample. At the same time, the area and depth of the survey result in a fairly large volume, $5 \times 10^7\ h^{-3}\,\mathrm{Mpc}^3$, analogous to that of the 2dFGRS at $z \sim 0.1$. Such a combination of sampling and depth is unique among current redshift surveys at $z > 0.5$. VIPERS is performed with the VIMOS multi-object spectrograph at the European Southern Observatory Very Large Telescope (Le Fèvre et al. 2002, 2003), at moderate resolution ($R = 210$), using the LR Red grism, providing a wavelength coverage of 5500-9500Å and a typical radial velocity error of 140 km sec^{-1}. The full VIPERS area is covered through a mosaic of 288 VIMOS pointings (192 in the W1 area and 96 in the W4 area). A complete description of the VIPERS survey, from the definition of the target sample to the actual spectra and redshift measurements, is presented in the parallel survey descrip-

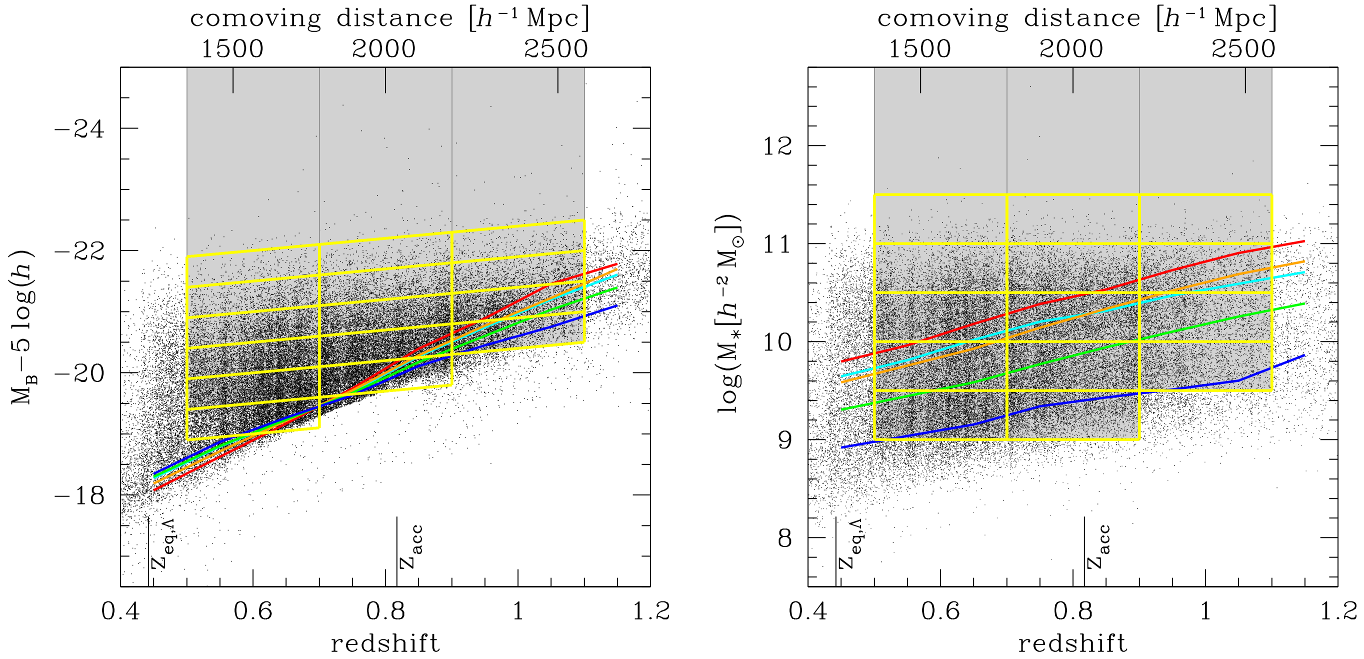

Fig. 1. Luminosity and stellar mass selection as a function of redshift. The black dots show the W1 and W4 VIPERS galaxies. Yellow lines surround the selected sub-samples. Solid lines show the 90% completeness levels for the whole galaxy population (cyan lines) and for galaxies of four different photometric types: red E/Sa (red lines), early spiral (magenta lines), late spiral (green lines) and irregular or starburst (blue lines). The B-band rest-frame magnitude limits in the left panel account for the average luminosity evolution of galaxies, as explained in the text. In the bottom axes, $z_{\mathrm{eq},\Lambda} \sim 0.44$ is the redshift of DM-DE equality and $z_{\mathrm{acc}} \sim 0.82$ is the redshift when the Universe started accelerating, according to ΛCDM predictions with the set of cosmological parameters adopted in this work.

tion paper (Guzzo et al. 2013), while a discussion of the survey data reduction and management infrastructure can be found in Garilli et al. (2012).

The PDR-1 galaxy catalogue includes 53,608 redshifts and corresponds to the reduced data frozen in the VIPERS database at the end of the 2011/2012 observing campaign. The 2PCF of PDR-1 galaxies and the first constraints on the growth rate from redshift-space distortions are presented in a parallel paper (de la Torre et al. 2013). A measurement of Ω_{M} using a novel clustering statistic is given in Bel et al. (2013). The galaxy stellar mass function is presented in Davidzon et al. (2013), while the luminosity function and the evolution of the colour bimodality is provided in Fritz et al. (2013). The PDR-1 galaxies are classified with a Support Vectors Machine algorithm in Malek et al. (2013), while an early subset of the spectra has been analyzed and classified through a Principal Component Analysis in Marchetti et al. (2013). Finally, the VIPERS redshift distribution has been used to measure the real-space galaxy power spectrum with colour-selected samples from the CFHTLS (Granett et al. 2012).

2.2. Luminosity and mass selection

We consider galaxy samples selected in three redshift ranges: $z \in [0.5, 0.7]$, $z \in [0.7, 0.9]$ and $z \in [0.9, 1.1]$. To investigate the luminosity and mass dependence of galaxy clustering, we use both threshold and binned sub-samples with different selections in B-band absolute magnitudes, M_{B}, and stellar masses, $M_\star$. The latter quantities have been estimated with a spectral energy distribution (SED) fitting technique, using the HYPERZMASS code (Bolzonella et al. 2000, 2010). Absolute magnitudes are measured using the B Buser filter in the AB system. More details about the SED fitting procedure are given in Davidzon et al. (2013).

Fig. 1 shows the sub-samples selected in this work. The adopted limits for the different sub-samples are highlighted by the grey area and the yellow solid lines. The black dots show the values of M_{B} (*left panel*) and $M_\star$ (*right panel*) for the W1 and W4 VIPERS galaxies, as a function of redshift. The B-band magnitude limits account for the average luminosity evolution of galaxies. Following Meneux et al. (2009), we model the average redshift evolution of galaxy magnitudes as $M_{\mathrm{B}}(z) = M_{\mathrm{B}}(0) + z$ (Ilbert et al. 2005; Zucca et al. 2009). Instead, for the stellar mass-selected sub-samples, we adopt the more conservative and widely used flat thresholds, as the redshift evolution of $M_\star$ is negligible up to $z \sim 1$ (Pozzetti et al. 2007, 2010; Davidzon et al. 2013). The solid coloured lines represent the 90% completeness levels for the whole galaxy population (cyan lines) and for galaxies of four different photometric types: red E/Sa (red lines), early spiral (magenta lines), late spiral (green lines) and irregular or starburst (blue lines) (see Davidzon et al. 2013, for more details). We do not use these completeness limits to investigate the dependence of galaxy clustering on spectral type, that we defer to a future work. These lines are displayed here to show that our magnitude-selected samples are all volume-limited irrespective of their colours, with the exception of the last redshift bin, where, due to our i band selection, we start losing the reddest galaxy population. However, the mass-selected samples are affected by the incompleteness of red galaxies. We will come back to this point in Section 3.4 and Appendix A.

Finally, in the bottom axes of Fig. 1, we mark $z_{\mathrm{eq},\Lambda}$, the redshift of DM-DE equality, and z_{acc}, the redshift when the

Universe started accelerating, according to ΛCDM predictions with the set of cosmological parameters adopted in this work. Clearly, the three redshift ranges considered for the present analysis probe different cosmic epochs, crossing the transition from deceleration to acceleration.

3. The two-point correlation function

In this section, we describe the methodology used to measure the galaxy 2PCF. In particular, we discuss our error estimates and sampling rate correction. Finally, we describe the method used to correct for mass incompleteness.

3.1. Clustering measurements

We quantify the spatial properties of the VIPERS galaxies using the 2PCF, $\xi(r)$. This function is implicitly defined as $dP = n^2[1+\xi(r)]dV_1 dV_2$, where dP is the probability of finding a pair of galaxies in the comoving volumes dV_1 and dV_2, separated by a comoving distance r, and n is the galaxy average number density. In the following, we will refer to real-space and redshift-space three-dimensional separations using the vectors $\boldsymbol{r}$ and $\boldsymbol{s}$, respectively.

To measure the function $\xi(s)$, we make use of the standard Landy & Szalay (1993) estimator:

$$\xi(s) = \frac{GG(s) - 2GR(s) + RR(s)}{RR(s)} \,, \tag{1}$$

where $GG(s)$, $GR(s)$ and $RR(s)$ are the normalized galaxy–galaxy, galaxy–random and random–random pairs, with spatial separation in the range $[s - \Delta s/2, s + \Delta s/2]$, respectively.

The random samples are generated in the Right Ascension-Declination plane, adopting the same geometric mask of the real data. We set $N_R = 30 N_{gal}$, where N_R is the number of random objects and N_{gal} is the number of galaxies in each sample. The latter values are reported in the fifth columns of Tables (1–4). The redshifts of the random objects are extracted from the smoothed radial distribution of the W1+W4 VIPERS galaxies, estimated in each luminosity and stellar mass sub-sample. Fig. 2 shows the whole comoving radial distances distribution of the W1 (green histograms) and W4 (yellow histograms) VIPERS galaxies. To smooth the total W1+W4 radial distribution, we use the non-parametric $V_{\rm max}$ method (see de la Torre et al. 2013, for more details). The blue solid line in Fig. 2 shows the result of the smoothing. A similar result can be obtained by filtering the distribution with a Gaussian kernel of $\sigma = 150 h^{-1}$ Mpc , as shown by the red line. The advantage of the $V_{\rm max}$ method is that it does not require us to make assumptions about the kernel. We have verified that all the results presented in this paper do not vary significantly when changing the smoothing scheme adopted.

3.2. Error estimate

The errors on the clustering measurements are estimated using a set of mock galaxy catalogues. For the luminosity-selected samples, we use data-calibrated HOD mocks, while for the stellar mass-selected samples we consider galaxy mocks built from the stellar-to-halo mass relation (SHMR) of Moster et al. (2013). We use 26 independent HOD and SHMR mock catalogues, both constructed by assigning galaxies to DM haloes of the MultiDark simulation, a large N-body run in the ΛCDM framework (Prada et al. 2012). A novel technique has been used to repopulate the MultiDark simulation with haloes of mass below the resolution limit (de la Torre & Peacock 2012) and thus to be able to simulate the faintest and less massive galaxies observed in VIPERS. A detailed description of the method used to construct our mock galaxy catalogues can be found in de la Torre et al. (2013). The covariance error matrix is estimated from the dispersion among the mock catalogues:

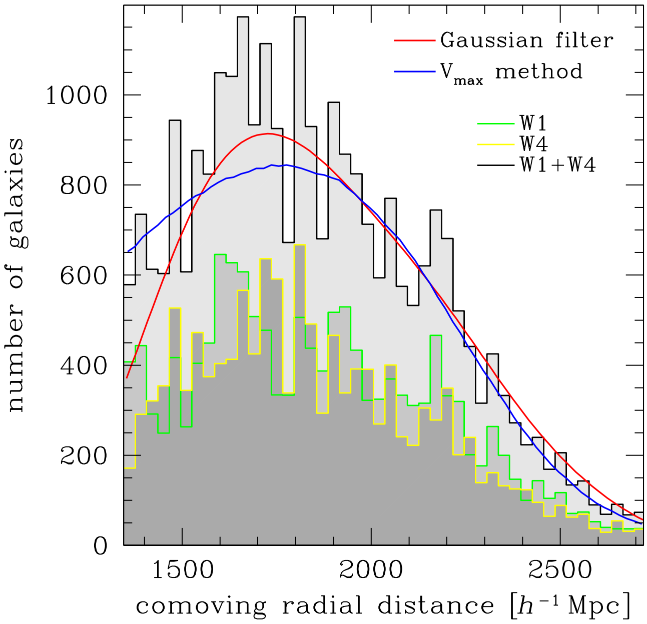

Fig. 2. Comoving radial distance distribution of the W1 and W4 VIPERS galaxy samples, shown with the green and yellow histograms, respectively. The red and blue lines show the total W1+W4 smoothed distribution, obtained by filtering the observed distribution with a Gaussian kernel of $\sigma = 150 h^{-1}$ Mpc and using the $V_{\rm max}$ method, respectively.

$$C_{ij} = \frac{1}{N-1} \sum_{k=1}^{N} \left(\bar{\xi}_i - \xi_i^k\right)\left(\bar{\xi}_j - \xi_j^k\right) \,, \tag{2}$$

where $\bar{\xi}_i$ is the mean value of the 2PCF, ξ_i^k, measured in each mock catalogue. The errors on the 2PCF are then obtained from the square root of the diagonal values of the covariance matrix, $\sigma_i = \sqrt{C_{ii}}$, that include both the Poissonian noise and the uncertainties due to the size of the volume explored, i.e. the sample variance. The luminosity and stellar mass dependence of the 2PCF errors is estimated measuring the covariance matrix in mock sub-samples with the same luminosity and stellar mass selection used for the real data.

3.3. Weighting the galaxy pairs

To properly account for the effects of sampling rate and colour selection, each galaxy has been weighted according to its sky position and redshift, using the following weight function:

$$\begin{aligned} w(Q,z) &= w_{CSR} \cdot w_{TSR} \cdot w_{SSR} \\ &= CSR^{-1}(z) \cdot TSR^{-1}(Q) \cdot SSR^{-1}(Q) \,. \end{aligned} \tag{3}$$

All of the weights in Eq. (3) are derived directly from the data. The Colour Sampling Rate, CSR, represents the completeness due to the colour selection. It mainly depends on redshift and can be modelled as $CSR(z) = 0.5[1 - \mathrm{erf}(7.405 - 17.465 \cdot z)]$, where erf is the error function $\mathrm{erf}(x) = 2/\sqrt{\pi}\int_0^x \exp(-t^2)dt$ (Guzzo et al. 2013; Coupon et al. 2013). The Target Sampling Rate, TSR, is defined as the fraction of galaxies in the photometric catalogue that have been spectroscopically targeted, $TSR = N_{\rm gal}(0 \le z_{\rm flag} \le 9.5)/N_{\rm target}$, where $z_{\rm flag}$ is the quality flag of the spectroscopic redshift measurement (see Guzzo et al. 2013, for more details on $z_{\rm flag}$). In addition, we have a 3.2% stellar contamination in the target sample, but the effect on the TSR is negligible. Finally, the Spectroscopic Success Rate, SSR, is defined as the fraction of the spectroscopically targeted galaxies for which a secure identification (i.e. high quality flag) has been obtained, $SSR = N_{\rm gal}(2 \le z_{\rm flag} \le 9.5)/N_{\rm gal}(0 \le z_{\rm flag} \le 9.5)$. Both the TSR and SSR depend on the VIMOS quadrant, Q, in which the galaxy has been observed. All the other possible dependencies, e.g. on redshift and magnitude, are comparatively smaller and can be neglected, as discussed in detail in de la Torre et al. (2013).

3.4. Proximity effects and mass incompleteness

The VIMOS multi-object spectrograph allows spectra for ∼400 galaxies to be obtained in a single pointing (Bottini et al. 2005); however, it is not possible to target galaxies that are close to each other along the dispersion direction. Thus, the highest density regions are under-sampled, resulting in a systematic underestimation of the correlation function, especially on small scales (Pollo et al. 2005; de la Torre et al. 2013). To estimate the impact of the proximity effect, we measure the mean ratio between the redshift-space 2PCF in two sets of 26 mock catalogues with and without the slit mask target selection algorithm applied. A similar test has been applied by Coil et al. (2008). The mock catalogues used here are constructed with a semi-analytic model (De Lucia & Blaizot 2007) on top of the Millennium simulation (Springel et al. 2005). To obtain a smoothed version of this ratio, we model it with an error function (see Fig. A.2 in Appendix A). Then, we multiply the measured redshift-space 2PCF by this smoothed ratio. As we find this correction to be almost independent on luminosity and stellar mass, we use the values obtained in our largest galaxy sample to correct all of our clustering measurements. At $z \lesssim 0.9$, the under-estimation of the 2PCF due to the proximity effect is ∼ 10% at scales $r \gtrsim 1\,h^{-1}\,\mathrm{Mpc}$, and increases slightly at smaller separations.

As shown in the right panel of Fig. 1, our mass-selected galaxy samples can be partially incomplete due to the limiting $i_{AB} < 22.5$ flux cut of VIPERS, missing galaxies with high mass-to-light ratio. To correct for this effect, we would have to know what are the clustering properties of the galaxies that are missing in each of our samples. This can only be inferred using galaxy formation models both complete in mass and realistically describing the formation and evolution of faint galaxies.

Following what has already been done in previous studies (see e.g. Meneux et al. 2008, 2009), we implement a correction method based on a similar strategy as described above for the proximity effect. Specifically, the correction is derived by measuring the ratio between the mean redshift-space 2PCF of two sets of mock catalogues, one complete in mass (down to $\sim 10^8 M_\odot$) and the other one magnitude-limited at $i_{AB} < 22.5$. According to the semi-analytic model considered here, the high mass-to-light ratio galaxies that are missed in our samples are faint red objects, that are predicted to be more clustered than the average population. Hence, the stellar mass incompleteness is expected to introduce a scale-dependent clustering suppression, up to ∼50% at scales $\lesssim 1\,h^{-1}\,\mathrm{Mpc}$, for the redshift-space 2PCF.

This correction assumes that different types of mock galaxies have clustering properties that match those of the real objects. However, this is only partially true. It is known that the model considered here overpredicts the abundance of faint and red galaxies. In addition, while the clustering of blue galaxies is well reproduced, the mock red galaxies appear more clustered than in real data (de la Torre et al. 2011; Cucciati et al. 2012). For the above reasons, such a model-dependent correction should be applied with caution. In the following, we will show our clustering measurements without correcting for stellar mass incompleteness. Nevertheless, in Tables 3–4, we provide our results obtained both with and without this correction, to directly show what is the expected effect according to the semi-analytic model considered.

More details about these two corrections for the proximity effect and mass incompleteness are provided in Appendix A.

3.5. Projected and real-space correlations and galaxy bias

To correct for redshift-space distortions due to galaxy peculiar velocities, and derive the 2PCF in real-space, $\xi(r)$, we first measure the clustering as a function of the two distances perpendicular and parallel to the line-of-sight, $\xi(r_p, \pi)$, using the Landy & Szalay (1993) estimator. Then, we integrate along the line of sight, π, as follows:

$$w_p(r_p) = 2\int_0^\infty d\pi'\,\xi(r_p, \pi')\,. \tag{4}$$

The real-space 2PCF can then be estimated by *deprojecting* the function $w_p(r_p)$ (Davis & Peebles 1983; Saunders et al. 1992), as follows:

$$\xi(r) = -\frac{1}{\pi}\int_r^\infty dr'_p \frac{dw_p(r'_p)/dr_p}{\sqrt{r'^2_p - r^2}}\,. \tag{5}$$

To facilitate the comparison with previous studies, we do not use Eq. 5, but model the function $\xi(r)$ as a single power-law:

$$\xi(r) = \left(\frac{r}{r_0}\right)^{-\gamma}\,. \tag{6}$$

With the above assumption, Eq. (4) can be solved analytically:

$$w_p(r_p) = r_p\left(\frac{r_0}{r_p}\right)^\gamma \frac{\Gamma(\frac{1}{2})\Gamma(\frac{\gamma-1}{2})}{\Gamma(\frac{\gamma}{2})}\,, \tag{7}$$

where Γ is the Euler's Gamma function. Hence, a power-law fit to $w_p(r_p)$ provides r_0 and γ for the real-space correlation function $\xi(r)$. Finally, the scale-dependent galaxy bias can be estimated as:

$$b(r) = \sqrt{\frac{\xi(r)}{\xi_{\rm m}(r)}}\,, \tag{8}$$

where $\xi_{\rm m}(r)$ is the matter 2PCF, that we derive using the software CAMB (Lewis & Bridle 2002), which exploits the HALOFIT routine (Smith et al. 2003) to reproduce the non-linear evolution of the matter correlation function [1].

---

[1] Alternatively, the bias function can be also estimated directly from the projected correlation function, as a function of the direction perpendicular to the line-of-sight, i.e. $b(r_p) = \sqrt{w_p(r_p)/w_p^{\rm m}(r_p)}$.

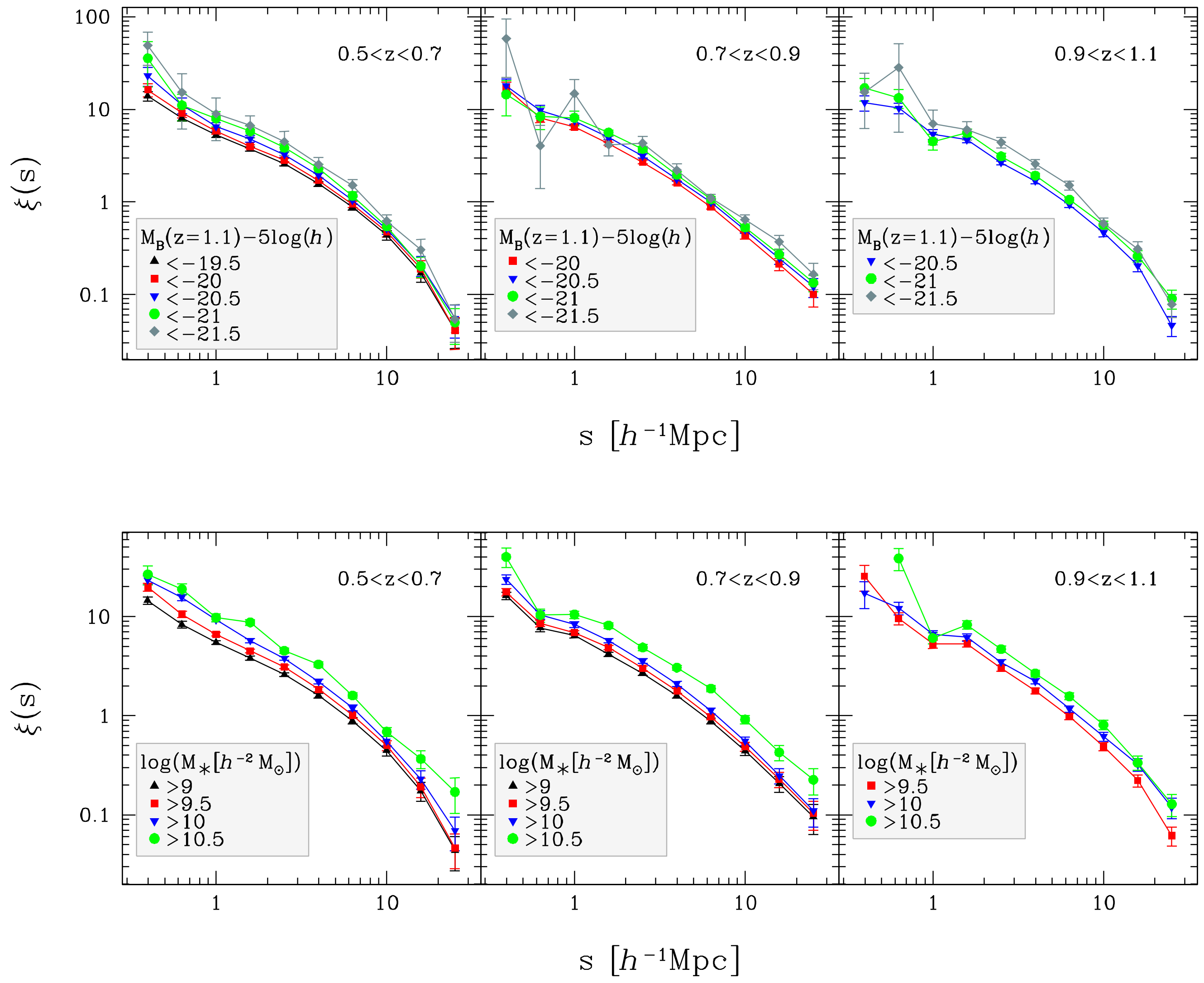

Fig. 3. 2PCF of VIPERS galaxies as a function of B-band absolute magnitude (*upper panels*) and stellar mass (*bottom panels*). The error bars are the square root of the diagonal values of the covariance matrix given by Eq. 2. Absolute magnitudes are given in the AB system.

4. Results

In this section, we present our results on the luminosity and stellar mass dependence of galaxy clustering and galaxy bias, and compare our results with those of previous studies.

4.1. Redshift-space and projected 2PCF

Fig. 3 shows the redshift-space 2PCF of VIPERS galaxies, $\xi(s)$, as a function of B-band absolute magnitude (*upper panels*) and stellar mass (*bottom panels*), in the three redshift ranges $z \in [0.5, 0.7]$, $z \in [0.7, 0.9]$ and $z \in [0.9, 1.1]$. The function $\xi(s)$ has been estimated using Eq. (1), while the error bars are the square root of the diagonal values of the covariance matrix, given by Eq. (2).

To derive the real-space 2PCF and directly compare the VIPERS clustering with previous data, we estimate the projected correlation function using Eq. 4. We integrate $\xi(r_p, \pi)$ up to $\pi_{\max} = 30\ h^{-1}$ Mpc. As we have verified, this choice represents a convenient compromise between robustness and the need to exclude noisy bins at large separations. The projected 2PCF of VIPERS galaxies is shown in Fig. 4. The upper and lower panels show, respectively, the luminosity and stellar mass dependence of $w_p(r_p)$, as indicated by the labels. The solid lines show the best-fit power-law models, given by Eq. 7, that we obtain fitting the correlation functions in the interval $0.2 < r_p[h^{-1}\,\mathrm{Mpc}] < 20$. The results presented in this work are robust with respect to the scale range used for the fit, except for the most luminous and massive galaxy samples. We can see in Fig. 4 that the power-law model does not describe well the small-scale behaviour of $w_p(r_p)$ for the most massive galaxies. This steepening in the amplitude of the correlation function on scales below $1h^{-1}$ Mpc can be interpreted in the framework of the halo model as due to the larger fraction of satellite galaxies in the massive haloes, creating a prominent one-halo term in the correlation function.

We find a clear luminosity and stellar mass segregation in galaxy clustering at all redshifts considered. This result is in agreement with previous findings, as discussed in detail in the

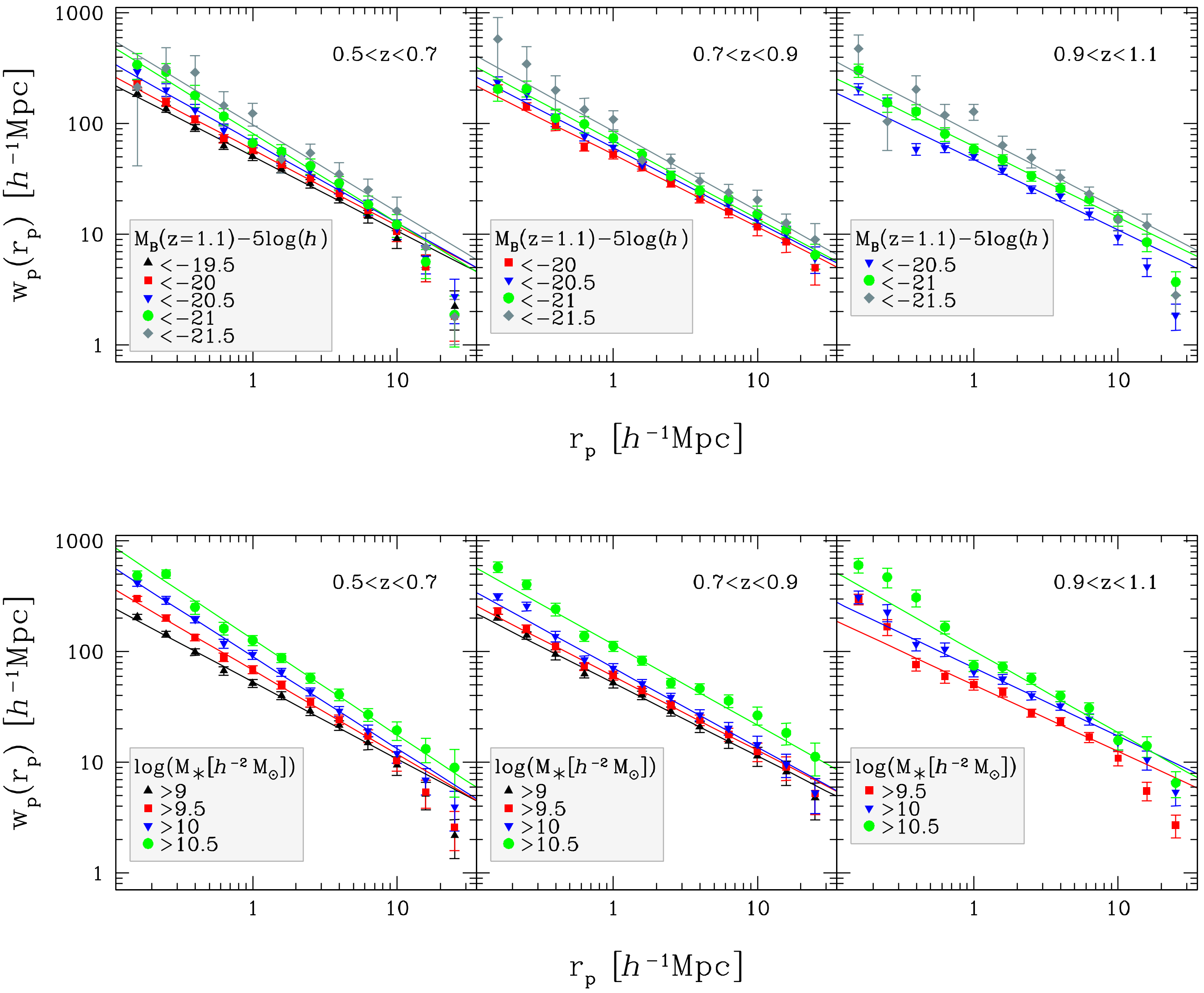

Fig. 4. Projected correlation function of VIPERS galaxies as a function of B-band absolute magnitude (*upper panels*) and stellar mass (*bottom panels*). The solid lines show the best-fit power-law models, obtained by fitting the correlation functions in the interval $0.2 < r_p[h^{-1}\,\mathrm{Mpc}] < 20$.

next section, and provides new strong constraints on galaxy formation models in the intermediate redshift Universe. The clustering measurements presented in Fig. 3 and 4 refer to threshold galaxy samples, as indicated by the labels. Our measurements on the galaxy clustering in both threshold and binned galaxy samples are given in Tables 1–4. Specifically, we provide the best-fit parameters of the power-law model: the correlation length r_0 (sixth columns), and the slope γ (seventh columns). The errors on the best-fit parameters are derived from the scatter among the r_0 and γ values measured in the 26 independent mock VIPERS mocks.

4.2. Comparison to previous studies

In Fig. 5, we compare our VIPERS measurements with many previous data, both at low and at high redshift. The upper panels show the best-fit values of r_0 and γ as a function of the B-band magnitude. Following Pollo et al. (2006), we normalize the median magnitudes of each galaxy sample to the corresponding values of the characteristic magnitude of the Schechter luminosity function, M_B^*, obtained by fitting the values of $M_B^*(z)$ given by Ilbert et al. (2005). With this method, we can properly compare samples at different redshifts, taking into account the mean brightening of galaxies due to their evolution.

Blue squares, red diamonds and green circles refer to our VIPERS constraints estimated at $z \in [0.5, 0.7]$, $z \in [0.7, 0.9]$ and $z \in [0.9, 1.1]$, respectively. A clear luminosity evolution of the clustering length, r_0, is evident at all redshifts. We can see that r_0 increases with time between $z \sim 1$ and $z \sim 0.6$. Moreover, there is some evidence that r_0 grows faster for faint galaxies with respect to the bright ones.

The black and grey symbols of Fig. 5 show previous measurements of the same quantity at different redshifts. Solid symbols refer to data taken in redshift ranges similar to ours, while open symbols are for data at lower or higher redshifts. For the local Universe, we consider the data from Zehavi et al. (2011) and Norberg et al. (2002). Zehavi et al. (2011) measured the luminosity dependence of galaxy clustering using the Sloan Digital

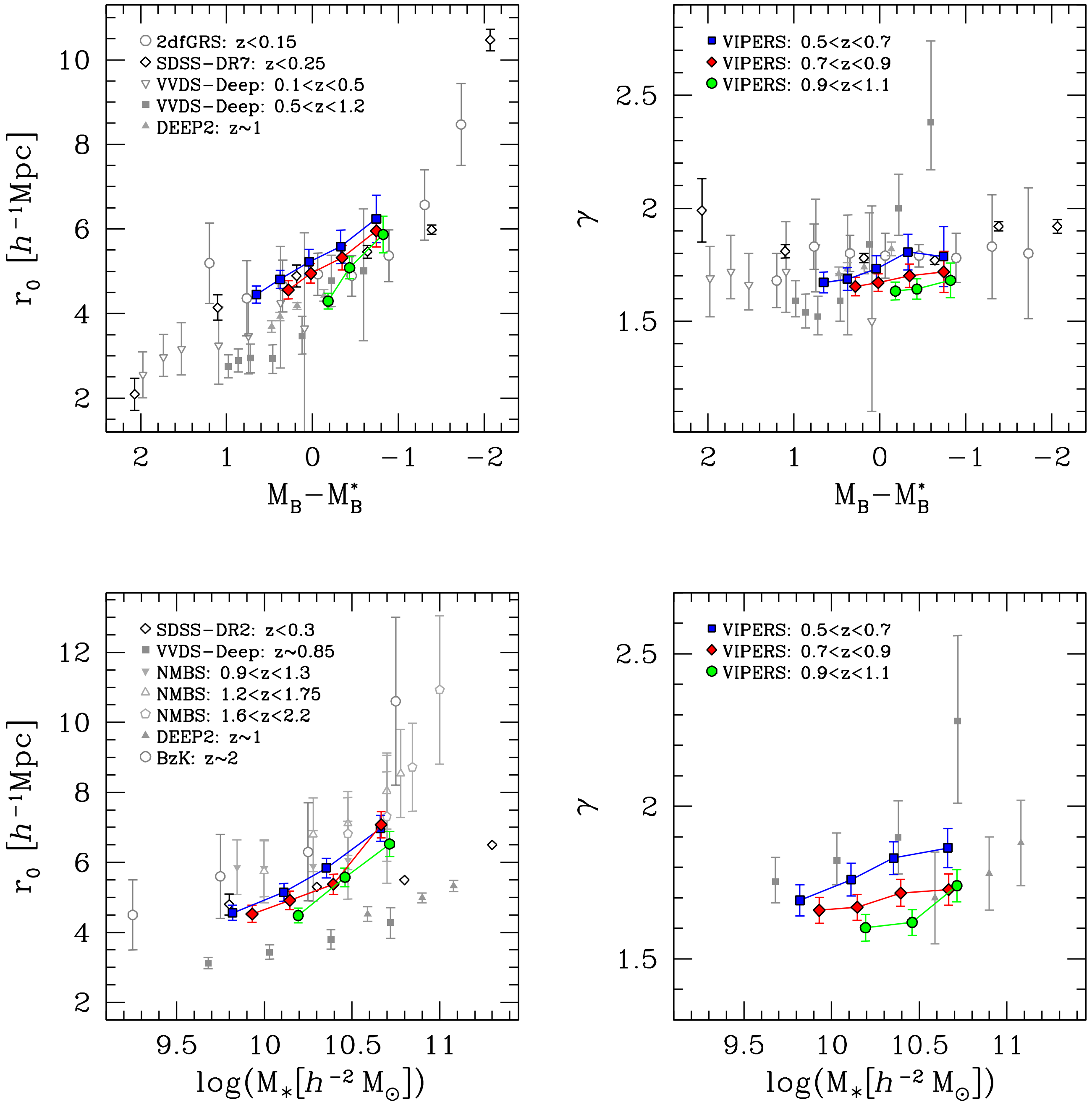

Fig. 5. Best-fit values of the correlation length, r_0, (*left panels*) and slope, γ, (*right panels*), as a function of B-band absolute magnitude (*upper panels*) and stellar mass (*bottom panels*). VIPERS constraints, obtained in threshold samples at $z \in [0.5, 0.7]$, $z \in [0.7, 0.9]$ and $z \in [0.9, 1.1]$ are shown, respectively, by blue squares, red diamonds and green circles, as indicated by the labels. The remaining grey symbols refer to measurements based on data from other surveys, reported here for comparison: *upper panels* – DSS-DR7 data from Zehavi et al. (2011), 2dfGRS data from Norberg et al. (2002), VVDS-Deep data from Pollo et al. (2006) and DEEP2 data from Coil et al. (2006); *lower panels* – SDSS-DR2 data from Li et al. (2006), VVDS-Deep data from Meneux et al. (2008), NMBS data from Wake et al. (2011), DEEP2 data from Mostek et al. (2012) and BzK data from Lin et al. (2012).

Sky Survey Seventh Data Release (SDSS-DR7), with volume-limited galaxy samples up to $z = 0.25$. Their results are shown by black open diamonds. Norberg et al. (2002) used the 2dF Galaxy Redshift Survey (2dFGRS) to measure the galaxy clustering up to $z = 0.15$. Dark grey open dots are used in Fig. 5 to display their measurements. Grey open rotated triangles and solid squares are the VIMOS-VLT Deep Survey (VVDS) clustering measurements at $0.1 < z < 0.5$ and $0.5 < z < 1.2$, respectively (Pollo et al. 2006). Finally, the grey solid triangles show the DEEP2 Galaxy Redshift Survey results at $z \sim 1$ from Coil et al. (2006). The latter two clustering measurements are at redshifts similar to VIPERS.

The bottom panels of Fig. 5 show the stellar mass dependence of r_0 and γ. We compare our results to data

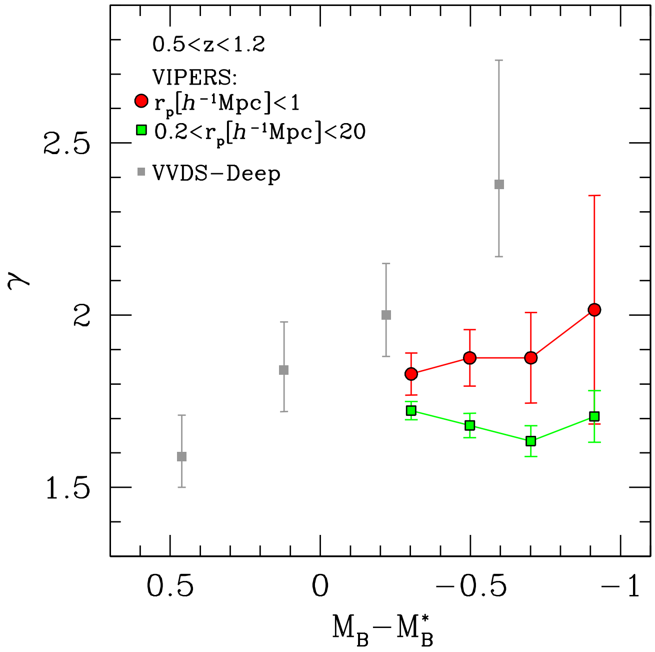

Fig. 6. Best-fit values of the VIPERS correlation slope, γ, as a function of luminosity. Green and red points show the VIPERS γ values obtained fitting $w_p(r_p)$ in $0.2 < r_p[h^{-1}\,\mathrm{Mpc}\,] < 20$ and $r_p < 2\ h^{-1}\,\mathrm{Mpc}$, respectively. Grey squares refer to the VVDS-Deep measurements in volume-limited samples.

from SDSS (Li et al. 2006), VVDS-Deep (Meneux et al. 2008), NMBS (Wake et al. 2011), DEEP2 (Mostek et al. 2012) and BzK (Lin et al. 2012). The best-fit clustering lengths from SDSS-DR2 data in the local Universe (Li et al. 2006) have been fitted by Mostek et al. (2012) and shown here by black open diamonds. The measurements at intermediate redshifts similar to VIPERS are shown by grey squares, that represent the VVDS-Deep results obtained by Meneux et al. (2008) at $z \sim 0.85$, by grey triangles, that show the DEEP2 measurements at $z \sim 1$ from Mostek et al. (2012), and by grey solid rotated triangles, that show the clustering measurements by Wake et al. (2011), using NMBS photometric redshifts in the range $0.9 < z < 1.3$, obtained with a fixed slope $\gamma = 1.6$. All the remaining grey symbols refer to higher redshift data. Open triangles and pentagons refer to the Wake et al. (2011) data at the two redshift ranges $1.2 < z < 1.75$ and $1.6 < z < 2.2$, respectively. Finally, the dark grey circles show the r_0 values estimated from the angular clustering analysis of BzK-selected star-forming galaxies at $z \sim 2$, for a fixed slope of $\gamma = 1.8$.

The general picture that emerges from these previous studies is that the clustering correlation length depends significantly on both luminosity and stellar mass, increasing monotonically from faint and low massive objects to luminous and massive ones, while the clustering slope remains fairly constant. It is interesting to note that for the intrinsically brightest samples, $M_B > M_B^*$, the clustering amplitude r_0 does not evolve significantly from $z \sim 1$ measurements of VVDS and DEEP2 to the local references of 2dFGRS and SDSS. The same behaviour is seen in VIPERS: we find little evolution in the most luminous bin. The VIPERS data allow us to track r_0 with precision over a range of luminosities from $z = 0.5 - 1.1$, and we find that the evolution becomes more significant at fainter luminosities. A possible interpretation of this result is that the most luminous galaxies at $z \sim 1$ were already almost as strongly clustered as they are now. With the three redshift slices of VIPERS we can observe the slow accumulation of these structures from $z \sim 1.1$ to $z \sim 0.5$.

On the other hand, when it comes to dependence of clustering on stellar mass, not all previous measurements are consistent. In particular, as it can be noted in the bottom left panel of Fig. 5, there is a big scatter between previous measurements, even when they probe similar redshift ranges. Clustering lengths at $z \sim 1$ found in the VVDS-Deep and DEEP2 surveys are significantly lower not only than the local measurements from the SDSS-DR7, but also than the values found by NMBS at $0.9 < z < 2.2$ and by the BzK at $z \sim 2$. Our estimates of r_0 are higher than the VVDS-Deep and DEEP2 ones, in the stellar mass range considered, while they fairly agree with all the other data.

The differences are likely to arise from a combination of systematic effects. The surveys considered in Fig. 5 are characterised by different properties, e.g. the methods for mass estimation, the cosmological parameters adopted to assess the distances and the selection criteria. The latter certainly introduce the most relevant effects, as different surveys can be affected by stellar mass incompleteness to varying degrees. In particular, the VIPERS mass-selected samples contain on average much brighter galaxies than VVDS and DEEP2, due to VIPERS higher flux selection cut.

Moreover, as the power-law model does not describe perfectly the data, measurements obtained fitting over different ranges could produce different values of the fit parameters. This effect is expecially significant for the most massive bins, where the shape of $w_p(r_p)$ is the furthest from a power-law and, thus, most sensitive to the range, binning and choice of points used for fitting. Finally, the impact of sample variance has been estimated with different techniques, and it might be underestimated in some cases.

The VIPERS clustering slope is almost constant, considering the estimated errors, around $\gamma \sim 1.7 - 1.8$, with only tentative evidences of a slight luminosity and redshift evolution. This is in overall agreement with all previous data, except for the relation measured in VVDS-Deep. Using the data from the VVDS-Deep Survey, Pollo et al. (2006) found a significant steepening of the correlation slope from $\gamma \sim 1.6$ at $< M_\mathrm{B} >= 19.6$, to $\gamma \sim 2.4$ at $< M_\mathrm{B} >= -21.3$, fitting $w_p(r_p)$ for separation $< 10\ h^{-1}\,\mathrm{Mpc}$ in their high-redshift range $0.5 < z < 1.2$ (see the grey squares in the upper right panel of Fig. 5).

To directly compare with VVDS data, we measure the VIPERS 2PCF in the same redshift range used by Pollo et al. (2005), $0.5 < z < 1.2$. In this way, any possible effect due to the intrinsic evolution in the VVDS broad redshift slice is present also in our measurements. We consider four volume-limited samples, with the following B-band magnitude thresholds $M_B(z = 1.2) - 5\log(h) < -21, -21.25, -21.5, -21.75$. The best-fit values of γ are shown in Fig. 6, compared to the VVDS-Deep measurements in volume-limited samples (grey squares). To investigate the scale dependence of the clustering slope, we compare the γ values obtained fitting $w_p(r_p)$ in the interval $0.2 < r_p[h^{-1}\,\mathrm{Mpc}\,] < 20$ (green points), and considering only small scales, $r_p < 1\ h^{-1}\,\mathrm{Mpc}$ (red points). The proximity effect caused by the one-pass strategy used in VIPERS is corrected with the method described in Section 3.3 and Appendix A. We are confident that the correction recovers the shape of the correlation function on small scales to within 5% (de la Torre et al. 2013).

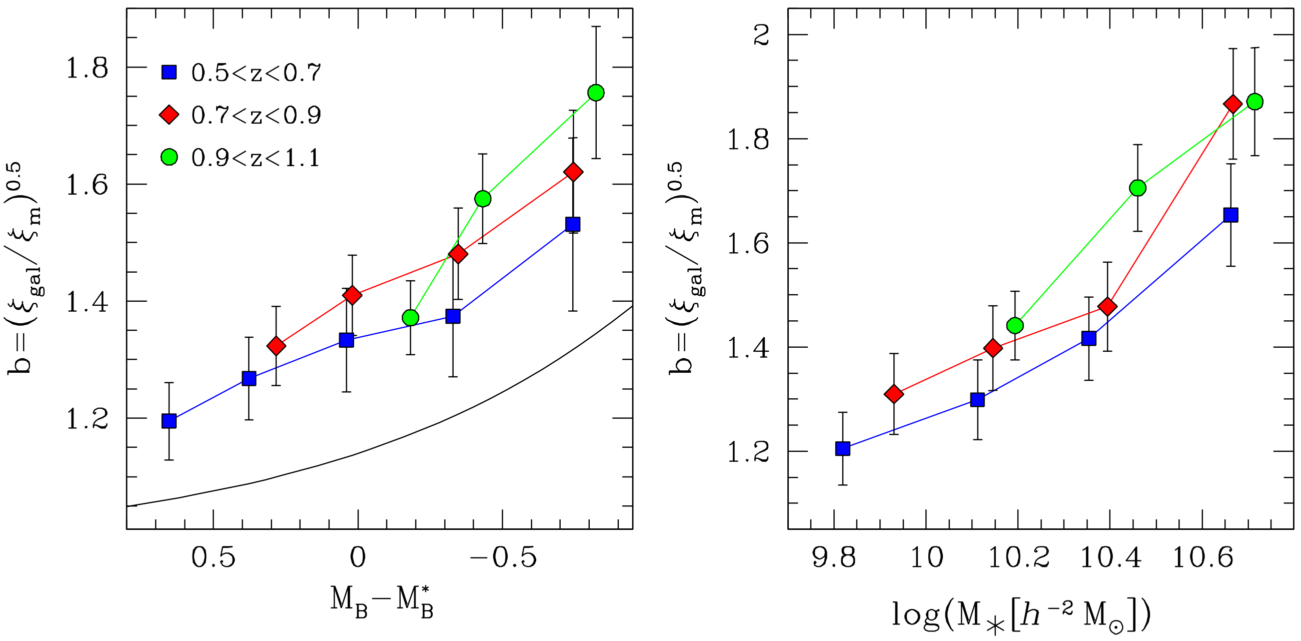

Fig. 7. Bias of VIPERS galaxies, averaged over the range [5 – 10] h^{-1} Mpc , as a function of B-band absolute magnitude (*left panel*) and stellar mass (*right panel*). The coloured symbols used for VIPERS measurements are the same as in Fig. 5. The black solid line in the left panel shows the fitted bias function by Zehavi et al. (2011).

When the 2PCF is fit on scales up to $20h^{-1}$ Mpc , γ appears almost constant at the value $\sim$ 1.7, as in Fig. 6, while if we fit only the small scales, γ results to be larger and slightly increasing, from $\gamma \sim 1.8$ at $\langle M_B - M_B^* \rangle \sim -0.3$, to $\gamma \sim 2$ at $\langle M_B - M_B^* \rangle \sim -0.9$. The VIPERS clustering slope is still lower than the VVDS one at high luminosities, though the mismatch is not large (below 2σ significance).

In conclusion, we find that the steeping of the slope in VVDS can be partly attributed to the range of scales used in the fit. However, the root cause of the discrepancy with VIPERS is probably due to sample variance in VVDS.

4.3. The galaxy bias

In this subsection, we present our estimates of the large-scale bias of VIPERS galaxies. We infer the scale-dependent bias, $b(r)$, using Eq. 8. Then, we average $b(r)$ in the range $5 < r[h^{-1}\,\mathrm{Mpc}\,] < 20$, where the galaxy bias is fairly constant. We assume a flat ΛCDM model with the matter density parameter $\Omega_M = 0.25$, the baryon density parameter $\Omega_b = 0.045$, the scalar spectral index $n_s = 1$ and the power spectrum normalization $\sigma_8 = 0.8$. A full HOD formalism would be necessary to properly describe the bias relation between galaxies and DM at different scales. However, at large scales, the bias obtained from the ratio of the galaxy correlation function to that of matter is consistent with that obtained using HOD modelling (see e.g. Zehavi et al. 2011).

In Fig. 7, we present the galaxy bias estimated in each threshold VIPERS sample, as a function of B-band absolute magnitude (left panel) and stellar mass (right panel). The error bars show the scatter among the bias values measured in the mock catalogues. The values of the bias and its error in each VIPERS sample are reported in Tables 1–4. The galaxy biasing estimated here depends on the assumed cosmological model through both σ_8 and Ω_M. The amplitude of galaxy bias scales linearly with σ_8^{-1}. The latter is known with an error of ~2%, only just negligible when compared to uncertainties in our bias parameter (~4%). Uncertainties on Ω_M, which is constrained in the interval ~ 0.22 – 0.28, also have an impact. Varying its input value in that range induces a ~2% shift in the estimated bias. On the other hand, *relative* bias between different galaxy types (e.g. the ratio between any two bias values reported in the tables), is almost model-independent.

Fig. 7 provides a compact view of the dependence of VIPERS clustering on luminosity and stellar mass. More luminous and massive galaxies appear more strongly biased than fainter and less massive ones, at all redshifts considered. At fixed luminosity and stellar mass, the bias function increases with redshift, while the amplitude of the 2PCF decreases (see Fig. 5). In the left panel of Fig. 7, the black solid line shows the luminosity dependence of the galaxy bias in the local Universe, estimated by Zehavi et al. (2011) using the SDSS-DR7 data (see also Norberg et al. 2001; Tegmark et al. 2004, for similar results). We note that the shape of the local bias results are broadly consistent with our findings at intermediate redshifts, while the normalisation is lower as predicted by evolution models (see e.g. Tegmark & Peebles 1998; Blanton et al. 2000; Pillepich et al. 2010).

A more detailed investigation on the scale dependence of the VIPERS galaxy bias derived with the deprojection method (see e.g. Marulli et al. 2012) and with a full HOD approach is deferred to a future work, while the non-linearity of the biasing function is presented in Di Porto et al. (2013).

4.4. Comparison to theoretical models

To provide a first theoretical interpretation of our measurements in a cosmological context, we compare the VIPERS cluster-

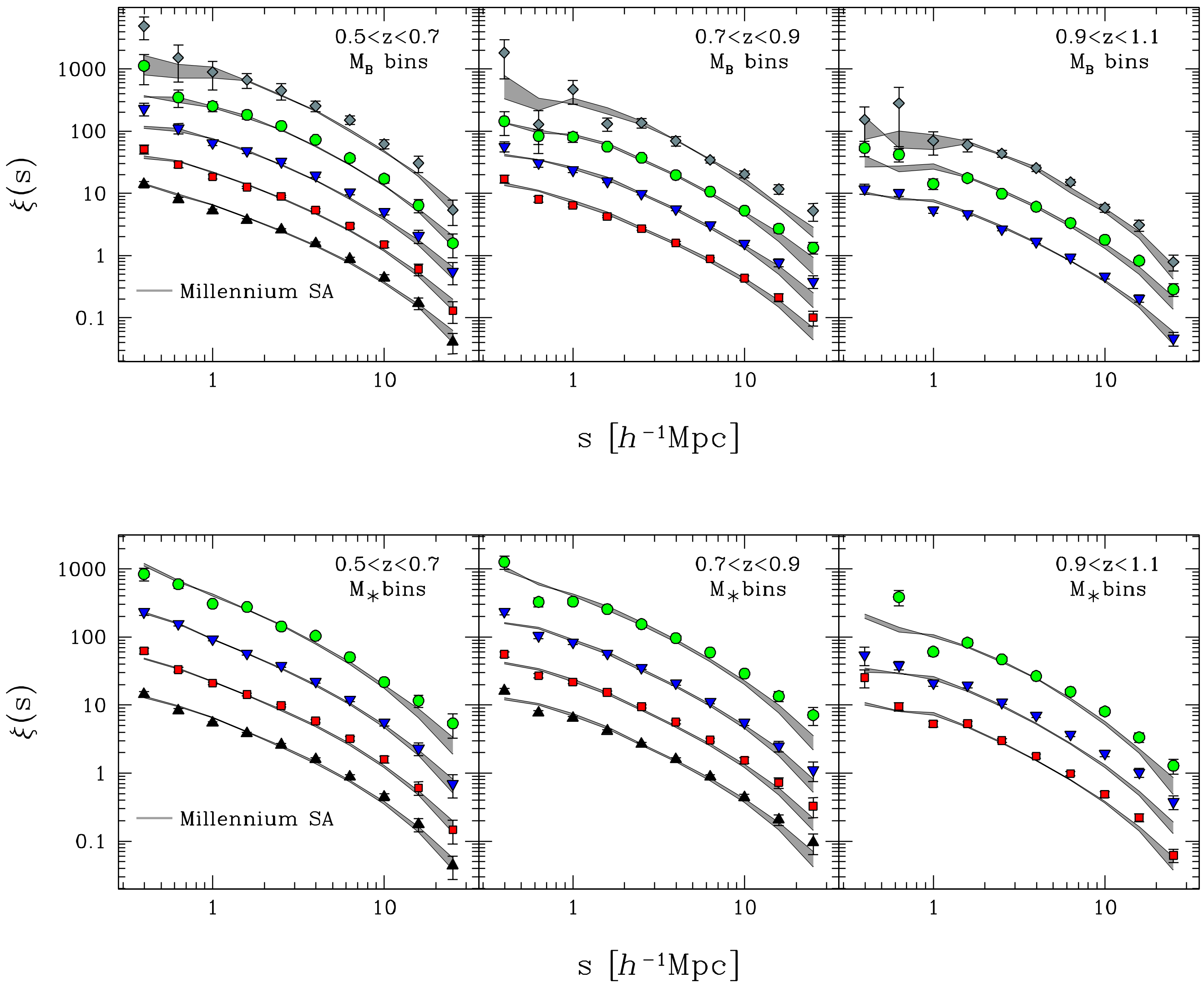

Fig. 8. Redshift-space 2PCF of VIPERS galaxies compared to theoretical expectations, as a function of B-band magnitude (*upper panels*) and stellar mass (*bottom panels*). The coloured symbols used for VIPERS measurements are the same as in Fig. 3. The grey shaded areas show the 2PCF measured in two large galaxy mock catalogues, constructed with the Munich semi-analytic model. The 2PCFs in different sub-samples are offset by 0.5 dex, starting from the lower luminosity and stellar mass samples, for visual clarity.

ing presented in previous sections with predictions of a standard galaxy formation model. The result is shown in Fig. 8, that compares the redshift-space 2PCF of VIPERS galaxies, measured in threshold samples of different luminosities (upper panels) and stellar masses (lower panels), with the theoretical predictions of the Munich semi-analytic model (Blaizot et al. 2005; De Lucia & Blaizot 2007). The coloured symbols used for VIPERS measurements are the same as in Fig. 3, while the grey shaded areas show the 2PCF measured in two large galaxy mock catalogues. The correlations in different sub-samples are offset by 0.5 dex, starting from the lower luminosity and stellar mass samples, for visual clarity. The Munich semi-analytic model, already introduced in Section 3.4 to calibrate the corrections for the proximity effect and stellar mass incompleteness, has been developed on the outputs of the Millennium Run, a large N-body DM simulation of the ΛCDM cosmological framework (Springel et al. 2005).

As it can be seen, our measurements can be understood within the standard ΛCDM+semi-analytic framework. Both the luminiosity and stellar mass dependence of the VIPERS clustering appear in overall good agreement with theoretical expectations, though we note that the more luminous and massive VIPERS galaxies are slightly more clustered than the semi-analytic ones, expecially at high redshift. However, we also remark that the value of $\sigma_8 = 0.9$, assumed in the Millennium simulation, is quite higher with respect to the most recent cosmological constraints (see e.g. de la Torre et al. 2011, for more discussions). If the Millennium predictions were rescaled accordingly, the agreement would slightly worsen. A detailed comparison between our measurements and theoretical predictions from different galaxy formation models is beyond the scope of the present paper, and it will be fully investigated in a future work.

5. Summary and conclusions

In this work, we studied how galaxy clustering depends on luminosity and stellar mass, in the redshift range $0.5 < z < 1.1$. To quantify the effect, we measured the redshift-space 2PCF of VIPERS galaxies in the first data release, PDR-1, and derived the real-space clustering and bias assuming a power-law form for the projected correlation function. Errors were estimated using a set of mock HOD and SHMR catalogues mimicking the characteristics and the observational selections of the VIPERS dataset.

The main results of this work can be summarised as follows:

- We confirm with unprecedented precision at $z = 0.5 - 1.1$ a monotonic increase of the clustering length r_0, both as a function of B-band magnitude and stellar mass, in all the three redshift ranges considered. On the contrary, the clustering slope, γ, appears quite constant when derived in the range $0.2 < r_p[h^{-1}\,\mathrm{Mpc}] < 20$.
- The dependence of the clustering length r_0 on luminosity is steepest at high redshift. In terms of the evolution of r_0 with redshift, we find that there is only a weak trend for the highest luminosity galaxies, while significant evolution in r_0 is found in the lower luminosity samples.
- VIPERS measurements are broadly consistent with previous studies, while establishing a bridge from the local references to the high-redshift Universe. However, we find a difference at the 2-σ level with previous VVDS-Deep and DEEP2 measurements at $z \sim 1$; we attribute this disagreement mainly to different stellar mass incompleteness levels in these catalogues with respect to VIPERS.
- We provide an estimate of galaxy bias, averaged over the range $[5 - 20]\ h^{-1}\,\mathrm{Mpc}$, as a function of luminosity, stellar mass and redshift, assuming a standard flat ΛCDM framework. The results are consistent with the predictions of hierarchical galaxy formation, although we will devote future work to testing evolution models in detail.

The measurements of the 2PCF presented here represent a considerable advancement over past surveys at $z \sim 1$. The large volume of VIPERS ensures that sample variance is subdominant. Furthermore, we have modelled the measurement covariance utilising mock surveys that account for both astrophysical and observational effects in detail. The results constitute new, stringent constraints on the galaxy 2PCF over a broad range of luminosities and stellar mass to be used as references against which to test models of cosmology and galaxy formation at redshifts $0.5 - 1.1$.

Acknowledgments

We acknowledge the crucial contribution of the ESO staff for the management of service observations. In particular, we are deeply grateful to M. Hilker for his constant help and support of this program. Italian participation to VIPERS has been funded by INAF through PRIN 2008 and 2010 programs. LG acknowledges support of the European Research Council through the Darklight ERC Advanced Research Grant (# 291521). OLF acknowledges support of the European Research Council through the EARLY ERC Advanced Research Grant (# 268107). Polish participants have been supported by the Polish Ministry of Science (grant N N203 51 29 38), the Polish-Swiss Astro Project (co-financed by a grant from Switzerland, through the Swiss Contribution to the enlarged European Union), the European Associated Laboratory Astrophysics Poland-France HECOLS and a Japan Society for the Promotion of Science (JSPS) Postdoctoral Fellowship for Foreign Researchers (P11802). GDL acknowledges financial support from the European Research Council under the European Community's Seventh Framework Programme (FP7/2007-2013)/ERC grant agreement n. 202781. WJP and RT acknowledge financial support from the European Research Council under the European Community's Seventh Framework Programme (FP7/2007-2013)/ERC grant agreement n. 202686. WJP is also grateful for support from the UK Science and Technology Facilities Council through the grant ST/I001204/1. EB, FM and LM acknowledge the support from grants ASI-INAF I/023/12/0 and PRIN MIUR 2010-2011. CM is grateful for support from specific project funding of the *Institut Universitaire de France* and the LABEX OCEVU.

Table 1. Properties of the selected VIPERS sub-samples in threshold luminosity bins. The best-fit values of the clustering normalization, r_0, and slope, γ, have been obtained fitting $w_p(r_p)$ in $0.2 < r_p[h^{-1}\,\mathrm{Mpc}\,] < 20$. The errors are from the scatter among the HOD VIPERS mocks. The bias values assume a flat ΛCDM model with $\Omega_\mathrm{M} = 0.25$ and $\sigma_8 = 0.8$.

redshift range	meadian redshift	magnitude range $M_B(z=1.1) - 5\log(h)$	median magnitude $M_B(z=1.1) - 5\log(h)$	N_{gal}	r_0 $[h^{-1}\,\mathrm{Mpc}\,]$	γ	bias
$[0.5, 0.7]$	0.62	< -19.5	-19.87	17473	4.45 ± 0.21	1.67 ± 0.05	1.19 ± 0.07
$[0.5, 0.7]$	0.62	< -20.0	-20.15	12432	4.81 ± 0.22	1.69 ± 0.05	1.27 ± 0.07
$[0.5, 0.7]$	0.62	< -20.5	-20.49	7472	5.22 ± 0.30	1.73 ± 0.06	1.33 ± 0.09
$[0.5, 0.7]$	0.62	< -21.0	-20.86	3599	5.58 ± 0.39	1.81 ± 0.08	1.37 ± 0.10
$[0.5, 0.7]$	0.62	< -21.5	-21.28	1236	6.24 ± 0.56	1.79 ± 0.13	1.53 ± 0.15
$[0.7, 0.9]$	0.79	< -20.0	-20.41	14442	4.56 ± 0.22	1.65 ± 0.04	1.32 ± 0.07
$[0.7, 0.9]$	0.80	< -20.5	-20.68	9469	4.95 ± 0.23	1.67 ± 0.04	1.41 ± 0.07
$[0.7, 0.9]$	0.80	< -21.0	-21.05	4605	5.32 ± 0.29	1.70 ± 0.05	1.48 ± 0.08
$[0.7, 0.9]$	0.80	< -21.5	-21.45	1619	5.95 ± 0.38	1.72 ± 0.09	1.62 ± 0.11
$[0.9, 1.1]$	0.97	< -20.5	-21.00	5018	4.29 ± 0.19	1.63 ± 0.04	1.37 ± 0.06
$[0.9, 1.1]$	0.98	< -21.0	-21.25	3035	5.08 ± 0.26	1.64 ± 0.05	1.57 ± 0.08
$[0.9, 1.1]$	0.99	< -21.5	-21.65	1123	5.87 ± 0.43	1.68 ± 0.08	1.76 ± 0.11

Table 2. Properties of the selected VIPERS sub-samples in binned luminosity bins. Parameters and errors are as in Table 1.

redshift range range	meadian redshift	magnitude range $M_B(z=1.1) - 5\log(h)$	median magnitude $M_B(z=1.1) - 5\log(h)$	N_{gal}	r_0 $[h^{-1}\,\mathrm{Mpc}\,]$	γ	bias
$[0.5, 0.7]$	0.62	$[-20.5, -19.5]$	-19.51	10001	3.92 ± 0.19	1.65 ± 0.05	1.09 ± 0.06
$[0.5, 0.7]$	0.62	$[-21.0, -20.0]$	-19.95	8833	4.58 ± 0.21	1.66 ± 0.05	1.23 ± 0.07
$[0.5, 0.7]$	0.62	$[-21.5, -20.5]$	-20.40	6236	5.00 ± 0.29	1.72 ± 0.06	1.29 ± 0.09
$[0.5, 0.7]$	0.62	$[-22.0, -21.0]$	-20.83	3334	5.35 ± 0.36	1.78 ± 0.08	1.34 ± 0.10
$[0.5, 0.7]$	0.62	$[-22.5, -21.5]$	-21.27	1207	6.29 ± 0.59	1.80 ± 0.13	1.53 ± 0.14
$[0.7, 0.9]$	0.78	$[-21.0, -20.0]$	-20.19	9837	4.08 ± 0.21	1.61 ± 0.05	1.23 ± 0.07
$[0.7, 0.9]$	0.80	$[-21.5, -20.5]$	-20.59	7850	4.71 ± 0.24	1.67 ± 0.04	1.35 ± 0.07
$[0.7, 0.9]$	0.80	$[-22.0, -21.0]$	-21.01	4246	5.20 ± 0.31	1.68 ± 0.05	1.47 ± 0.08
$[0.7, 0.9]$	0.80	$[-22.5, -21.5]$	-21.45	1586	5.96 ± 0.40	1.71 ± 0.10	1.63 ± 0.11
$[0.9, 1.1]$	0.96	$[-21.5, -20.5]$	-20.86	3895	3.63 ± 0.15	1.64 ± 0.04	1.19 ± 0.05
$[0.9, 1.1]$	0.98	$[-22.0, -21.0]$	-21.21	2777	4.90 ± 0.29	1.65 ± 0.04	1.52 ± 0.08
$[0.9, 1.1]$	0.99	$[-22.5, -21.5]$	-21.64	1091	5.98 ± 0.43	1.70 ± 0.08	1.77 ± 0.11

Table 3. Properties of the selected VIPERS sub-samples in threshold stellar mass bins. The quantities r_0^C, γ^C and bias^C are the clustering normalization, slope and linear bias corrected for the stellar mass incompleteness, respectively. The other parameters and errors are the same as in Table 1.

redshift range	meadian redshift	stellar mass range $[h^{-2}\,M_\odot]$	median stellar mass $[h^{-2}\,M_\odot]$	N_{gal}	r_0 $[h^{-1}\,\mathrm{Mpc}\,]$	γ	bias	r_0^C	γ^C	bias^C
$[0.5, 0.7]$	0.61	> 9.0	9.82	17102	4.55 ± 0.22	1.69 ± 0.05	1.20 ± 0.07	4.99	1.70	1.30
$[0.5, 0.7]$	0.62	> 9.5	10.11	11567	5.14 ± 0.25	1.76 ± 0.05	1.30 ± 0.08	5.70	1.77	1.42
$[0.5, 0.7]$	0.62	> 10.0	10.35	6880	5.84 ± 0.28	1.83 ± 0.05	1.42 ± 0.08	6.01	1.83	1.46
$[0.5, 0.7]$	0.62	> 10.5	10.66	2151	6.97 ± 0.37	1.86 ± 0.06	1.65 ± 0.10	6.97	1.86	1.66
$[0.7, 0.9]$	0.78	> 9.0	9.93	15020	4.53 ± 0.25	1.66 ± 0.04	1.31 ± 0.08	4.73	1.67	1.35
$[0.7, 0.9]$	0.79	> 9.5	10.15	11346	4.92 ± 0.26	1.67 ± 0.04	1.40 ± 0.08	5.41	1.69	1.51
$[0.7, 0.9]$	0.79	> 10.0	10.39	6884	5.37 ± 0.29	1.72 ± 0.04	1.48 ± 0.09	5.87	1.73	1.59
$[0.7, 0.9]$	0.79	> 10.5	10.67	2498	7.08 ± 0.38	1.73 ± 0.05	1.87 ± 0.11	7.22	1.73	1.90
$[0.9, 1.1]$	0.97	> 9.5	10.19	4558	4.48 ± 0.21	1.60 ± 0.04	1.44 ± 0.07	4.51	1.62	1.44
$[0.9, 1.1]$	0.97	> 10.0	10.46	2857	5.57 ± 0.27	1.62 ± 0.04	1.71 ± 0.08	5.78	1.65	1.74
$[0.9, 1.1]$	0.97	> 10.5	10.71	1281	6.52 ± 0.35	1.74 ± 0.05	1.87 ± 0.10	6.78	1.76	1.93

Table 4. Properties of the selected VIPERS sub-samples in binned stellar mass bins. Parameters and errors are as in Table 3.

redshift range	meadian redshift	stellar mass range $[h^{-2}\,M_\odot]$	median stellar mass $[h^{-2}\,M_\odot]$	N_{gal}	r_0 $[h^{-1}\,\mathrm{Mpc}]$	γ	bias	r_0^C	γ^C	bias^C
[0.5, 0.7]	0.62	[9.5, 10.5]	9.88	7487	5.47 ± 0.31	1.82 ± 0.06	1.34 ± 0.09	6.36	1.84	1.53
[0.5, 0.7]	0.62	[10.0, 11.0]	10.19	2952	6.54 ± 0.32	1.87 ± 0.05	1.55 ± 0.09	6.73	1.87	1.60
[0.5, 0.7]	0.62	[10.5, 11.5]	10.66	2150	6.93 ± 0.36	1.87 ± 0.06	1.64 ± 0.10	6.95	1.87	1.65
[0.7, 0.9]	0.79	[9.5, 10.5]	9.92	7410	5.11 ± 0.32	1.69 ± 0.06	1.43 ± 0.10	6.25	1.69	1.70
[0.7, 0.9]	0.79	[10.0, 11.0]	10.19	3353	6.31 ± 0.33	1.72 ± 0.05	1.70 ± 0.10	6.95	1.73	1.84
[0.7, 0.9]	0.79	[10.5, 11.5]	10.67	2497	7.04 ± 0.37	1.73 ± 0.05	1.86 ± 0.11	7.21	1.73	1.90
[0.9, 1.1]	0.97	[9.5, 10.5]	9.98	2942	5.21 ± 0.35	1.60 ± 0.06	1.63 ± 0.09	5.63	1.60	1.74
[0.9, 1.1]	0.97	[10.0, 11.0]	10.25	1620	6.23 ± 0.30	1.77 ± 0.05	1.78 ± 0.09	6.52	1.78	1.85

References

Abbas, U., de la Torre, S., Le Fèvre, O., et al. 2010, Mon. Not. R. Astron. Soc., 406, 1306

Abbas, U. & Sheth, R. K. 2006, Mon. Not. R. Astron. Soc., 372, 1749

Adelberger, K. L., Steidel, C. C., Pettini, M., et al. 2005, Astrophys. J., 619, 697

Alcock, C. & Paczynski, B. 1979, Nature, 281, 358

Bel, J. et al. 2013, Astron. Astrophys., submitted

Benoist, C., Maurogordato, S., da Costa, L. N., Cappi, A., & Schaeffer, R. 1996, Astrophys. J., 472, 452

Blaizot, J., Wadadekar, Y., Guiderdoni, B., et al. 2005, Mon. Not. R. Astron. Soc., 360, 159

Blanton, M., Cen, R., Ostriker, J. P., Strauss, M. A., & Tegmark, M. 2000, Astrophys. J., 531, 1

Bolzonella, M., Kovač, K., Pozzetti, L., et al. 2010, Astron. Astrophys., 524, A76

Bolzonella, M., Miralles, J.-M., & Pelló, R. 2000, Astron. Astrophys., 363, 476

Bottini, D., Garilli, B., Maccagni, D., et al. 2005, Publ. Astron. Soc. Pac., 117, 996

Brown, M. J. I., Dey, A., Jannuzi, B. T., et al. 2003, Astrophys. J., 597, 225

Brown, M. J. I., Webster, R. L., & Boyle, B. J. 2000, Mon. Not. R. Astron. Soc., 317, 782

Budavári, T., Connolly, A. J., Szalay, A. S., et al. 2003, Astrophys. J., 595, 59

Christodoulou, L., Eminian, C., Loveday, J., et al. 2012, Mon. Not. R. Astron. Soc., 425, 1527

Coil, A. L., Newman, J. A., Cooper, M. C., et al. 2006, Astrophys. J., 644, 671

Coil, A. L., Newman, J. A., Croton, D., et al. 2008, Astrophys. J., 672, 153

Cole, S. et al. 2005, Mon. Not. R. Astron. Soc., 362, 505

Coupon, J. et al. 2013, ArXiv e-prints

Cucciati, O., De Lucia, G., Zucca, E., et al. 2012, Astron. Astrophys., 548, A108

Daddi, E., Röttgering, H. J. A., Labbé, I., et al. 2003, Astrophys. J., 588, 50

Davidzon, I. et al. 2013, Astron. Astrophys., submitted

Davis, M. & Geller, M. J. 1976, Astrophys. J., 208, 13

Davis, M., Meiksin, A., Strauss, M. A., da Costa, L. N., & Yahil, A. 1988, Astrophys. J. Lett., 333, L9

Davis, M. & Peebles, P. J. E. 1983, Astrophys. J., 267, 465

de la Torre, S., Meneux, B., De Lucia, G., et al. 2011, Astron. Astrophys., 525, A125

de la Torre, S. & Peacock, J. A. 2012, ArXiv e-prints

de la Torre, S. et al. 2013, Astron. Astrophys., submitted

De Lucia, G. & Blaizot, J. 2007, Mon. Not. R. Astron. Soc., 375, 2

Di Porto, C. et al. 2013, ArXiv e-prints

Einasto, M. 1991, Mon. Not. R. Astron. Soc., 252, 261

Eisenstein, D. J. et al. 2005, Astrophys. J., 633, 560

Fritz, A. et al. 2013, Astron. Astrophys., submitted

Garilli, B., Paioro, L., Scodeggio, M., et al. 2012, Publ. Astron. Soc. Pac., 124, 1232

Giovanelli, R., Haynes, M. P., & Chincarini, G. L. 1986, Astrophys. J., 300, 77

Granett, B. R., Guzzo, L., Coupon, J., et al. 2012, Mon. Not. R. Astron. Soc., 421, 251

Guo, H., Zehavi, I., Zheng, Z., et al. 2012, ArXiv e-prints

Guzzo, L., Bartlett, J. G., Cappi, A., et al. 2000, Astron. Astrophys., 355, 1

Guzzo, L., Strauss, M. A., Fisher, K. B., Giovanelli, R., & Haynes, M. P. 1997, Astrophys. J., 489, 37

Guzzo, L. et al. 2013, Astron. Astrophys., submitted

Hamilton, A. J. S. 1988, Astrophys. J. Lett., 331, L59

Hildebrandt, H., Pielorz, J., Erben, T., et al. 2009, Astron. Astrophys., 498, 725

Ilbert, O., Tresse, L., Zucca, E., et al. 2005, Astron. Astrophys., 439, 863

Kaiser, N. 1987, Mon. Not. R. Astron. Soc., 227, 1

Landy, S. D. & Szalay, A. S. 1993, Astrophys. J., 412, 64

Le Fèvre, O., Mancini, D., Saisse, M., et al. 2002, The Messenger, 109, 21

Le Fèvre, O., Saisse, M., Mancini, D., et al. 2003, in Society of Photo-Optical Instrumentation Engineers (SPIE) Conference Series, Vol. 4841, Society of Photo-Optical Instrumentation Engineers (SPIE) Conference Series, ed. M. Iye & A. F. M. Moorwood, 1670–1681

Lee, K.-S., Giavalisco, M., Conroy, C., et al. 2009, Astrophys. J., 695, 368

Lee, K.-S., Giavalisco, M., Gnedin, O. Y., et al. 2006, Astrophys. J., 642, 63

Lewis, A. & Bridle, S. 2002, Phys. Rev. D, 66, 103511

Li, C., Kauffmann, G., Jing, Y. P., et al. 2006, Mon. Not. R. Astron. Soc., 368, 21

Lin, L., Dickinson, M., Jian, H.-Y., et al. 2012, Astrophys. J., 756, 71

Loh, Y.-S., Rich, R. M., Heinis, S., et al. 2010, Mon. Not. R. Astron. Soc., 407, 55

Loveday, J., Maddox, S. J., Efstathiou, G., & Peterson, B. A. 1995, Astrophys. J., 442, 457

Madgwick, D. S., Hawkins, E., Lahav, O., et al. 2003, Mon. Not. R. Astron. Soc., 344, 847

Malek, K. et al. 2013, Astron. Astrophys., submitted

Marchetti, A., Granett, B. R., Guzzo, L., et al. 2013, Mon. Not. R. Astron. Soc., 428, 1424

Marulli, F., Bianchi, D., Branchini, E., et al. 2012, Mon. Not. R. Astron. Soc., 426, 2566

Maurogordato, S. & Lachieze-Rey, M. 1991, Astrophys. J., 369, 30

McCracken, H. J., Ilbert, O., Mellier, Y., et al. 2008, Astron. Astrophys., 479, 321

Mellier, Y., Bertin, E., Hudelot, P., et al. 2008, http://terapix.iap.fr/cplt/oldSite/Descart/CFHTLS-T0005-Release.pdf

Meneux, B., Guzzo, L., de la Torre, S., et al. 2009, Astron. Astrophys., 505, 463

Meneux, B., Guzzo, L., Garilli, B., et al. 2008, Astron. Astrophys., 478, 299

Meneux, B., Le Fèvre, O., Guzzo, L., et al. 2006, Astron. Astrophys., 452, 387

Mostek, N., Coil, A. L., Cooper, M. C., et al. 2012, ArXiv e-prints

Moster, B. P., Naab, T., & White, S. D. M. 2013, Mon. Not. R. Astron. Soc., 428, 3121

Norberg, P., Baugh, C. M., Hawkins, E., et al. 2002, Mon. Not. R. Astron. Soc., 332, 827

Norberg, P., Baugh, C. M., Hawkins, E., et al. 2001, Mon. Not. R. Astron. Soc., 328, 64

Ouchi, M., Hamana, T., Shimasaku, K., et al. 2005, Astrophys. J. Lett., 635, L117

Percival, W. J., Cole, S., Eisenstein, D. J., et al. 2007, Mon. Not. R. Astron. Soc., 381, 1053

Percival, W. J. et al. 2010, Mon. Not. R. Astron. Soc., 401, 2148

Pillepich, A., Porciani, C., & Hahn, O. 2010, Mon. Not. R. Astron. Soc., 402, 191

Pollo, A., Guzzo, L., Le Fèvre, O., et al. 2006, Astron. Astrophys., 451, 409

Pollo, A., Meneux, B., Guzzo, L., et al. 2005, Astron. Astrophys., 439, 887

Pozzetti, L., Bolzonella, M., Lamareille, F., et al. 2007, Astron. Astrophys., 474, 443

Pozzetti, L., Bolzonella, M., Zucca, E., et al. 2010, Astron. Astrophys., 523, A13

Prada, F., Klypin, A. A., Cuesta, A. J., Betancort-Rijo, J. E., & Primack, J. 2012, Mon. Not. R. Astron. Soc., 423, 3018

Ross, A. J., Tojeiro, R., & Percival, W. J. 2011, Mon. Not. R. Astron. Soc., 413, 2078

Saunders, W., Rowan-Robinson, M., & Lawrence, A. 1992, Mon. Not. R. Astron. Soc., 258, 134

Scodeggio, M., Franzetti, P., Garilli, B., Le Fèvre, O., & Guzzo, L. 2009, The Messenger, 135, 13

Simpson, F. & Peacock, J. A. 2010, Phys. Rev. D, 81, 043512

Smith, R. E., Peacock, J. A., Jenkins, A., et al. 2003, Mon. Not. R. Astron. Soc., 341, 1311

Springel, V. et al. 2005, Nature, 435, 629

Swanson, M. E. C., Tegmark, M., Blanton, M., & Zehavi, I. 2008, Mon. Not. R. Astron. Soc., 385, 1635

Tegmark, M. & Peebles, P. J. E. 1998, Astrophys. J. Lett., 500, L79

Tegmark, M. et al. 2004, Astrophys. J., 606, 702

Wake, D. A., Whitaker, K. E., Labbé, I., et al. 2011, Astrophys. J., 728, 46

White, S. D. M., Frenk, C. S., Davis, M., & Efstathiou, G. 1987, Astrophys. J., 313, 505

Willmer, C. N. A., da Costa, L. N., & Pellegrini, P. S. 1998, Astron. J., 115, 869

Zehavi, I., Blanton, M. R., Frieman, J. A., et al. 2002, Astrophys. J., 571, 172

Zehavi, I., Eisenstein, D. J., Nichol, R. C., et al. 2005, Astrophys. J., 621, 22

Zehavi, I., Zheng, Z., Weinberg, D. H., et al. 2011, Astrophys. J., 736, 59

Zucca, E., Bardelli, S., Bolzonella, M., et al. 2009, Astron. Astrophys., 508, 1217

Appendix A: Correcting for stellar mass incompleteness and proximity effect

A possible method to correct the 2PCF measurements for stellar mass incompleteness is described in Section 3.4. We provide here more details on this procedure and quantify the impact on our meaurements. The method consists in measuring the 2PCF in two sets of mock galaxy catalogues, one set complete in stellar masses, while the other one with the same VIPERS $i_{AB} < 22.5$ flux cut. We use mock catalgoues constructed with the Munich semi-analytic galaxy formation model (Blaizot et al. 2005; De Lucia & Blaizot 2007), on top of the DM halo trees from the Millennium simulation (Springel et al. 2005). These catalogues are complete in stellar masses down to $\sim 10^8 M_\odot$. The red dots in Fig. A.1 show the mean ratio between the 2PCF in flux-limited and complete mocks, averaged over the 10 independent catalogues, while the error bars are the rms scatter. The

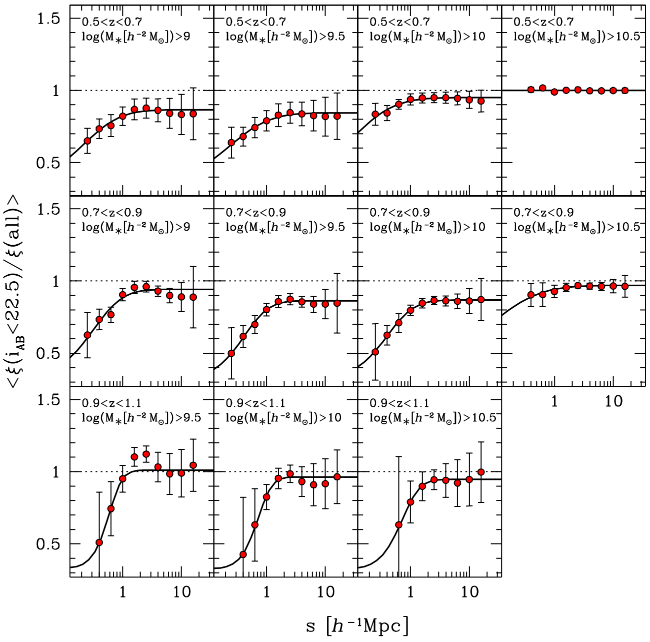

Fig. A.1. Ratio between the redshift-space 2PCF measured in flux-limited and complete semi-analytic mocks. The red dots show the clustering ratio averaged over 10 independent mock catalogues, while the error bars are the rms scatter. The black lines show the best-fit error function used to smooth these ratios.

results refer to different redshift and stellar mass limits, as explicitly indicated by the labels. According to the Munich model, the mass incompleteness introduces a clear scale-dependent reduction of clustering, mainly significant at scales $\lesssim 1\ h^{-1}$ Mpc. The black lines, that show the best-fit error functions used to smooth these ratios, represent the correction that we actually use to obtain the values of r_0^C, γ^C and bias^C reported in Tables (3–4). As already stressed in Section 3.4, since the mock red and faint galaxies are significantly more clustered than the observed ones, this model-dependent correction should be taken with caution.

As discussed in Section 3.3, due to our multi-object slit masks, it is not possible to observe galaxies that are too close to each other. This proximity effect introduces a further scale-dependent suppression in the 2PCF that we have to correct. We adopt the same strategy described above to correct for mass incompleteness, i.e. we measure the ratio between the redshift-space 2PCF in mock catalogues with and without the slit mask target selection algorithm applied (also see Coil et al. 2008). As before, the mock galaxy catalogues used here are constructed with the Munich semi-analytic galaxy formation model. Fig. A.2 shows the results of this method. The red dots are the mean values of this ratio as a function of luminosity, stellar mass and redshift, as reported in the labels. The error bars show the scatter between the mock samples. The black lines, as in Fig. A.1, show the error functions used to model these ratios. This correction results to be almost independent on luminosity and stellar mass, similar to the results of Coil et al. (2006). Thus, we decide to use the correction calibrated in our largest galaxy sample to correct all our clustering measurements. We notice that the systematic clustering suppression due to the proximity effect becomes less severe going to high redshift. More details can be found in de la Torre et al. (2013).

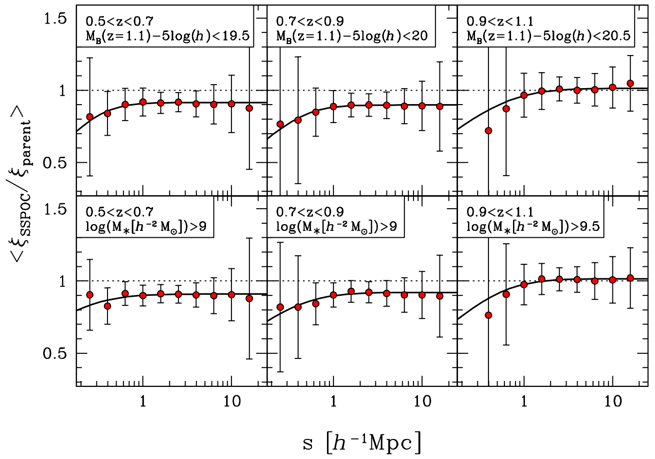

Fig. A.2. As Fig. A.1, except for the redshift-space 2PCF measured in mock catalogues with and without the slit mask target selection algorithm applied.

---

[1] Dipartimento di Fisica e Astronomia - Università di Bologna, viale Berti Pichat 6/2, I-40127 Bologna, Italy
[2] INAF - Osservatorio Astronomico di Bologna, via Ranzani 1, I-40127 Bologna, Italy
[3] INFN - Sezione di Bologna, viale Berti Pichat 6/2, I-40127 Bologna, Italy
[4] Dipartimento di Matematica e Fisica, Università degli Studi Roma Tre, via della Vasca Navale 84, 00146 Roma, Italy
[5] INFN - Sezione di Roma Tre, via della Vasca Navale 84, I-00146 Roma, Italy
[6] INAF - Osservatorio Astronomico di Roma, via Frascati 33, I-00040 Monte Porzio Catone (RM), Italy
[7] SUPA - Institute for Astronomy, University of Edinburgh, Royal Observatory, Blackford Hill, Edinburgh, EH9 3HJ, UK
[8] INAF - Osservatorio Astronomico di Brera, Via Brera 28, 20122 Milano, via E. Bianchi 46, 23807 Merate, Italy
[9] Dipartimento di Fisica, Università di Milano-Bicocca, P.zza della Scienza 3, I-20126 Milano, Italy
[10] Astronomical Observatory of the Jagiellonian University, Orla 171, 30-001 Cracow, Poland
[11] National Centre for Nuclear Research, ul. Hoza 69, 00-681 Warszawa, Poland
[12] INAF - Osservatorio Astronomico di Torino, 10025 Pino Torinese, Italy
[13] Aix Marseille Université, CNRS, LAM (Laboratoire d'Astrophysique de Marseille) UMR 7326, 13388, Marseille, France
[14] Canada-France-Hawaii Telescope, 65–1238 Mamalahoa Highway, Kamuela, HI 96743, USA
[15] Centre de Physique Théorique, UMR 6207 CNRS-Université de Provence, Case 907, F-13288 Marseille, France
[16] INAF - Istituto di Astrofisica Spaziale e Fisica Cosmica Milano, via Bassini 15, 20133 Milano, Italy
[17] Laboratoire Lagrange, UMR7293, Université de Nice Sophia-Antipolis, CNRS, Observatoire de la Côte d'Azur, 06300 Nice, France
[18] Institute of Astronomy and Astrophysics, Academia Sinica, P.O. Box 23-141, Taipei 10617, Taiwan
[19] INAF - Osservatorio Astronomico di Trieste, via G. B. Tiepolo 11, 34143 Trieste, Italy
[20] Institute of Physics, Jan Kochanowski University, ul. Swietokrzyska 15, 25-406 Kielce, Poland
[21] Department of Particle and Astrophysical Science, Nagoya University, Furo-cho, Chikusa-ku, 464-8602 Nagoya, Japan
[22] Institute d'Astrophysique de Paris, UMR7095 CNRS, Université Pierre et Marie Curie, 98 bis Boulevard Arago, 75014 Paris, France
[23] Universitätssternwarte München, Ludwig-Maximillians Universität, Scheinerstr. 1, D-81679 München, Germany
[24] Max-Planck-Institut für Extraterrestrische Physik, D-84571 Garching b. München, Germany
[25] Institute of Cosmology and Gravitation, Dennis Sciama Building, University of Portsmouth, Burnaby Road, Portsmouth, PO1 3FX, UK
[26] INAF - Istituto di Astrofisica Spaziale e Fisica Cosmica Bologna, via Gobetti 101, I-40129 Bologna, Italy
[27] INAF - Istituto di Radioastronomia, via Gobetti 101, I-40129 Bologna, Italy
[28] Università degli Studi di Milano, via G. Celoria 16, 20130 Milano, Italy